Modeling the Electromagnetic Field in Lossy Dielectrics Using Finite Elements and Vector Absorbing Boundary Conditions

Vassilios N. Kanellopoulos, *Member, IEEE,* and Jon P. Webb, *Member, IEEE*

***Abstract*—A new functional for the finite element method is described for the distribution of high-frequency electromagnetic fields in arbitrarily shaped, lossy dielectrics in 3D. The method uses a brick-shaped edge element (covariant-projection element) and a second-order, symmetric, vector absorbing boundary condition. Analytic solutions are available for the case of a plane wave incident on a lossy sphere, and these are used to show that the new method is capable of predicting the fields in and around the sphere to an average accuracy of 1–2%, even when the outer, absorbing boundary is no more than a third of a wavelength from the sphere.**

I. Introduction

THE FINITE element method (FEM) is a powerful and accurate technique for modeling electromagnetic problems of arbitrary geometries. As it is based on a partial differential equation, it requires volume discretization, i.e., division of the region of interest into smaller nonoverlapping subvolumes, the finite elements, on which a special mathematical procedure is applied [1]. The FEM solves for the stationary point of a functional F [2]. The whole mathematical procedure leads to a square, sparse, and symmetric (or Hermitian) matrix. The matrix size depends on the number of the finite elements into which the volume of interest has been discretized, and the polynomial order of the trial functions.

In vector problems, *edge elements* guarantee solutions free from the unreal spurious fields, which arise from the improper modeling of the irrotational fields. Spurious fields do not satisfy Maxwell's equations. Edge elements are tangentially continuous, and they can handle both sharp metallic corners and dielectric inhomogeneities without any extra effort [3]. *Covariant projection elements*, a type of curvilinear edge element, have also successfully been used in high-frequency vector problems [4]–[7], [10], [12]. Their advantages are referenced in [4], [5]. These elements have been used in this work.

Manuscript received March 16, 1994; revised August 8, 1994. This work was supported by the Natural Sciences and Engineering Research Council (NSERC) of Canada.

V. N. Kanellopoulos was with the Laboratoire de Génie Electrique de Paris, URA 127 CNRS, Ecole Supérieur d'Electricité, Universités Paris 6 et 11, F-91192 Gif-sur-Yvette, France. He is now with the Aristotle University of Thessaloniki (AUT), Thessaloniki, Greece.

J. P. Webb is with the Computational Analysis and Design Laboratory, Department of Electrical Engineering, McGill University, Montreal, P.Q., Canada H3A 2A7.

IEEE Log Number 9408563.

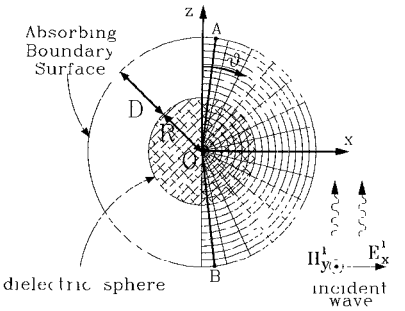

Fig. 1. An x-z cross-section of the 3D geometry. The gray area is the dielectric sphere of radius R, which is completely enclosed by the concentric absorbing boundary surface of radius $R + D$. The incident plane wave is x-polarized and z-traveling.

In open-boundary vector problems, e.g., 3D high-frequency electromagnetic scattering, it is impossible to discretize the unbounded infinite volume. For such problems, the FEM is frequently coupled to an integral equation condition (IEC) [8]. The FEM is used for the interior volume of interest, and the IEC takes care of the exterior infinite domain. This IEC is global and exact; however, it destroys the sparsity of the FE matrices, and frequently it suffers from singularities. An approximate local absorbing boundary condition (ABC) was recently proposed that could be used in partial differential equation techniques [13]. The symmetric version of this which renders it suitable to the FEM was developed and tested successfully [9], [10], [12]. This ABC is applied on a spherical absorbing boundary surface (ABS) that completely surrounds the discretized volume of interest; see Fig. 1. Its physical interpretation is that of an approximate impedance boundary condition for all the outgoing waves traveling through ABS. It is shown that for metallic scatterers and for outgoing waves, this technique constitutes a powerful tool in electromagnetic modeling, allowing the wide use of the FEM in unbounded problems [5].

This FE–ABC method was extended so that the ABS may not be a sphere, but rather a multisurface that consists of several planes completely enclosing the volume of interest [11]. The results presented showed very good accuracy in the far-field region, but their accuracy was not verified in the near-field region.

In this work, a simpler form of the functional F than that used in [11] is given, valid for metallic and dielectric objects in the presence of incident waves. A lossy dielectric

sphere was analyzed, and the calculation refers to the near-field region where the error is maximum. Only second-order ABC's have been used, since they were shown to be superior to the first-order ones [5], [10], [12].

II. Variational Formulation

In electromagnetic scattering, the total electric field $\boldsymbol{E}$ can be expressed as the sum of the incident $\boldsymbol{E}^i$ and the scattered $\boldsymbol{E}^s$ parts

$$\boldsymbol{E} = \boldsymbol{E}^i + \boldsymbol{E}^s, \tag{1}$$

and similarly for the magnetic field $\boldsymbol{H}$

$$\boldsymbol{H} = \boldsymbol{H}^i + \boldsymbol{H}^s. \tag{2}$$

Thus, in the presence of dielectrics, the two curl Maxwell's equations may be written as

$$\nabla \times \boldsymbol{H}^s = j\omega\epsilon_0\epsilon_r\boldsymbol{E}^s + \boldsymbol{J}_e \tag{3}$$

$$\nabla \times \boldsymbol{E}^s = -j\omega\mu_0\boldsymbol{H}^s \tag{4}$$

where j is the square root of minus one, ω is the angular frequency, ϵ_0 and μ_0 are the permittivity and permeability of free space, respectively, ϵ_r is the relative permittivity of medium, and $\boldsymbol{J}_e = j\omega\epsilon_0(\epsilon_r - 1)\boldsymbol{E}^i$ is the equivalent source current. Then the curl–curl equation is given by

$$\nabla \times \nabla \times \boldsymbol{E}^s - k_0^2\epsilon_r\boldsymbol{E}^s = k_0^2(\epsilon_r - 1)\boldsymbol{E}^i \tag{5}$$

where the free-space wavenumber k_0 is given by: $k_0 = \omega\sqrt{\epsilon_0\mu_0}$. On the exterior spherical absorbing boundary surface (ABS), the following second-order ABC is applied [5], [12]

$$\hat{\boldsymbol{a}}_r \times \nabla \times \boldsymbol{E}^s = \alpha\boldsymbol{E}_t^s + \beta(r)\{\nabla_t(\nabla \cdot \boldsymbol{E}_t^s) + \nabla \times \hat{\boldsymbol{a}}_r[\hat{\boldsymbol{a}}_r \cdot (\nabla \times \boldsymbol{E}^s)]\} \tag{6}$$

where $\hat{\boldsymbol{a}}_r$ is the radial unit vector, $\alpha = jk_0$, and $\beta = 1/(2jk_0 + 2/r)$. The subscript t denotes the tangential component to the ABS. The above ABC is approximate, valid for outward-propagating waves, and improves at a rate of r^{-5} [9]. For the curl–curl equation (5) and the second-order ABC, the functional F may be written as

$$\begin{aligned} F(\boldsymbol{E}^s) = \int_V \{&(\nabla \times \boldsymbol{E}^s)^2 - k_0^2\epsilon_r\boldsymbol{E}^{s^2} \\ &- 2k_0^2(\epsilon_r - 1)\boldsymbol{E}^i \cdot \boldsymbol{E}^s\}\, dV \\ &+ \int_S \{\alpha\boldsymbol{E}_t^{s^2} + \beta(r)[\hat{\boldsymbol{a}}_r \cdot (\nabla \times \boldsymbol{E}^s)]^2 \\ &- \beta(r)(\nabla \cdot \boldsymbol{E}_t^s)^2\}\, dS \end{aligned} \tag{7}$$

where $\boldsymbol{E}^s$ is the unknown scattered complex vector electric field, V is the volume of interest, and S is the ABS which should be in the air. The presence of the surface-divergence term in the surface integral in (7) requires that normal continuity of the field is imposed on ABS. This can be very easily done if the element edges on the ABS are collinear with lines of constant θ and ϕ [12]. The stationary point of F (7) gives

$$1) \quad \int_V [\delta\boldsymbol{E}^s \cdot (\nabla \times \nabla \times \boldsymbol{E}^s) - k_0^2\epsilon_r\delta\boldsymbol{E}^s \cdot \boldsymbol{E}^s - k_0^2(\epsilon_r - 1)\delta\boldsymbol{E}^s \cdot \boldsymbol{E}^i]\, dV = 0 \tag{8}$$

which, in fact, is the curl–curl equation (5), and

$$\begin{aligned} 2) \quad \int_S \{&\delta\boldsymbol{E}^s \cdot (\nabla \times \boldsymbol{E}^s \times \hat{\boldsymbol{a}}_r) + \beta(r) \\ &\cdot [\hat{\boldsymbol{a}}_r \cdot (\nabla \times \delta\boldsymbol{E}^s)][\hat{\boldsymbol{a}}_r \cdot (\nabla \times \boldsymbol{E}^s)] \\ &+ \alpha(\delta\boldsymbol{E}_t^s) \cdot \boldsymbol{E}_t^s - \beta(r)(\nabla \cdot \delta\boldsymbol{E}_t^s)(\nabla \cdot \boldsymbol{E}_t^s)\}\, dS = 0 \end{aligned} \tag{9}$$

which is the second-order ABC (6). The same results can be obtained using a weighted residual method.

III. The Lossy Dielectric Sphere

For an x-polarized and z-traveling plane wave, the electric field is given by

$$E_x^i = E_0 e^{-jk_0 z} = E_0 e^{-jk_0 r\cos(\theta)}$$

where E_0 is a constant. Let the center of a dielectric sphere of radius R be located at the origin of the coordinate axes. In the presence of the above incident wave, this sphere will create the following scattered electric field $\boldsymbol{E}^s$: 1) in the region (ϵ_0, μ_0), i.e., $r > R$ (derived from [14, (6–26), (6–100)])

$$E_r^s = \frac{E_0\cos(\phi)}{jk_0^2r^2}\sum_{n=1}^{\infty} n(n+1) \cdot b_n\hat{H}_n^{(2)}(k_0r)P_n^1(\cos(\theta)) \tag{10a}$$

$$E_\theta^s = -\frac{E_0\cos(\phi)}{k_0r} \cdot \left(\frac{1}{\sin(\theta)}\sum_{n=1}^{\infty} c_n\hat{H}_n^{(2)}(k_0r)P_n^1(\cos(\theta)) - \frac{1}{j}\sum_{n=1}^{\infty} b_n\hat{H}_n^{(2)'}(k_0r)\frac{\partial}{\partial\theta}P_n^1(\cos(\theta))\right) \tag{10b}$$

$$E_\phi^s = \frac{E_0\sin(\phi)}{k_0r} \cdot \left(\sum_{n=1}^{\infty} c_n\hat{H}_n^{(2)}(k_0r)\frac{\partial}{\partial\theta}P_n^1(\cos(\theta)) - \frac{1}{j\sin(\theta)}\sum_{n=1}^{\infty} b_n\hat{H}_n^{(2)'}(k_0r)P_n^1(\cos(\theta))\right); \tag{10c}$$

and 2) in the region (ϵ_r, μ_0), i.e., $r < R$ (derived from [14, (6-26), (6-112)])

$$E_r^s = \frac{E_0\cos(\phi)}{jk^2r^2}\sum_{n=1}^{\infty} n(n+1)d_n \cdot \hat{J}_n(kr)P_n^1(\cos(\theta)) - \cos(\phi)\sin(\theta)(E_0e^{-jk_0r\cos(\theta)}) \tag{11a}$$

$$E_\theta^s = -\frac{E_0\cos(\phi)}{k_0r} \cdot \left(\frac{1}{\sin(\theta)}\sum_{n=1}^{\infty} e_n\hat{J}_n(kr)P_n^1(\cos(\theta))\right.$$

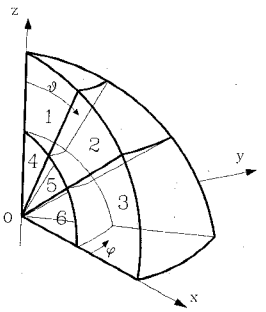

Fig. 2. Degenerate curvilinear brick elements touching the z axis and the origin 0.

$$- \frac{1}{j\sqrt{\epsilon_r}} \sum_{n=1}^{\infty} d_n \hat{J}_n'(kr) \frac{\partial}{\partial \theta} P_n^1(\cos(\theta)) \Bigg) - \cos(\theta)\cos(\phi)(E_0 e^{-jk_0 r\cos(\theta)}) \tag{11b}$$

$$E_\phi^s = \frac{E_0 \sin(\phi)}{k_0 r} \cdot \left(\sum_{n=1}^{\infty} e_n \hat{J}_n(kr) \frac{\partial}{\partial \theta} P_n^1(\cos(\theta)) - \frac{1}{j\sqrt{\epsilon_r}\sin(\theta)} \sum_{n=1}^{\infty} d_n \hat{J}_n'(kr) P_n^1(\cos(\theta)) \right) + \sin(\phi)(E_0 e^{-jk_0 r\cos(\theta)}) \tag{11c}$$

where ϵ_r can be complex, $k = \sqrt{\epsilon_r} k_0$, $\hat{J}_n(x) = \sqrt{\pi x/2}\, J_{n+\frac{1}{2}}(x)$, $\hat{H}_n^{(2)}(x) = \sqrt{\pi x/2}\, H_{n+\frac{1}{2}}^{(2)}(x)$, J_n is the Bessel function of the first kind of order n, $H_n^{(2)}$ is the Hankel function of second kind of order n [15], $P_n^1 = -(\partial P_n/\partial\theta)$, and P_n is the Legendre polynomial [15]. The prime denotes the derivatives with respect to $k_0 r$ or kr, respectively. The constants b_n, c_n, d_n, and e_n are the ones given in [14, (6-113)], but they have been multiplied by -1 for consistency.

IV. Results

The problem of the dielectric sphere scatterer in the presence of an incident plane wave was analyzed with the new method. The dielectric sphere was chosen because analytical solutions exist for this geometry. The geometry of the problem is shown in Fig. 1. Due to symmetries, only one quarter of the volume was modeled holding the following boundary conditions (see also Fig. 1):

Boundary Surface:	Boundary Condition:
$r = R + D$	Absorbing boundary condition
$\phi = 0°$	Magnetic wall
$\phi = 90°$	Electric wall

The finite elements used were curvilinear hexahedra, except those touching the z axis which were degenerate; see Fig. 2. Elements 2 and 3 are standard curvilinear hexahedra, element 4 is a curvilinear tetrahedron (i.e., a twice degenerate hexahedron), and the others are curvilinear pentahedra (i.e., once degenerate hexahedra).

TABLE I
The Four Cases Treated

	$\epsilon_r = (3.0, -2.0)$	$\epsilon_r = (20.0, -10.0)$
$R = 0.36\lambda_0$	case 1	case 2
$R = 0\ 477\lambda_0$	case 3	case 4

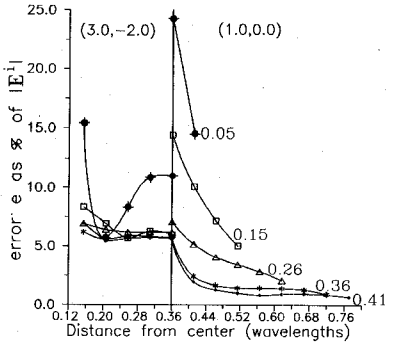

Fig. 3. Solution error versus r, which is the distance from the origin 0. The radius of the dielectric sphere is $R = 0.36\ \lambda_0$ and its relative permittivity $\epsilon_r = (3.0, -2.0)$. The solution error is the largest value of $e = |\boldsymbol{E}^s_{\rm FEM} - \boldsymbol{E}^s_{\rm exact}|$ over the volume modeled, expressed as a percentage of the magnitude of the incident electric field. The numbers at the right end of each curve indicate the distance D in free-space wavelengths (see also Fig. 1).

Four separate cases were treated: case 1, case 2, case 3, and case 4. In case 1 (low frequency, low dielectric), the dielectric sphere's radius was $R = 0.36\ \lambda_0$ (λ_0 is the free-space wavelength) and the relative permittivity was $\epsilon_r = (3.0, -2.0)$. In case 4 (higher frequency, higher dielectric), the sphere's radius was $R = 0.477\ \lambda_0$ and $\epsilon_r = (20.0, -10.0)$. See Table I for cases 2 and 3.

There were 14 and 8 elements in the θ and ϕ directions, respectively, one element every $0.05\ \lambda_0$ in the r direction for cases 1 and 2, and one element every $0.06\ \lambda_0$ for cases 3 and 4.

Figs. 3 and 4 show how the error changes in cases 1 and 2 as the ABS is moved outwards. The maximum field error shown is the largest value of

$$e = |\boldsymbol{E}^s_{\rm FEM} - \boldsymbol{E}^s_{\rm exact}| \tag{12}$$

over the volume modeled, expressed as a percentage of the magnitude of the incident electric field. The numbers at the right end of each curve indicate the distance D in free-space wavelengths (see also Fig. 1). The analytical expressions for the field (10)–(11) do not provide a unique value on the z axis, and they fail to converge in its vicinity. Therefore, no comparisons were made for these regions. It appears that there is not much improvement in the error inside the dielectric when the ABS is placed at a distance $D > 0.26\ \lambda_0$ away from the sphere, while outside, it continues to improve. This is because the same mesh density was used everywhere in the mesh, so the discretization error in the dielectric is bigger than that outside. This is also why the error inside the higher dielectric is a little bit higher than that in the low dielectric.

Fig. 5 shows the amplitude of the total electric field $\boldsymbol{E}$ along the line BA, at $\theta = 6.4286°$ and $\phi = 45°$(Fig. 1). The solid line represents the analytical results, and it was interpolated in the vicinity of 0 to give a continuous line. The ABS was set at a distance $D = 0.36\ \lambda_0$ away from the sphere. The average error throughout the mesh was about 1%. The

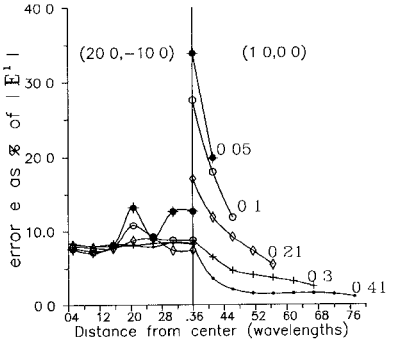

Fig. 4. Solution error versus r, which is the distance from the origin 0. The radius of the dielectric sphere is $R = 0.36\ \lambda_0$ and its relative permittivity $\epsilon_r = (20.0, -10.0)$. The solution error is the largest value of $e = |\boldsymbol{E}^s_{\mathrm{FEM}} - \boldsymbol{E}^s_{\mathrm{exact}}|$ over the volume modeled, expressed as a percentage of the magnitude of the incident electric field. The numbers at the right end of each curve indicate the distance D in free-space wavelengths (see also Fig. 1).

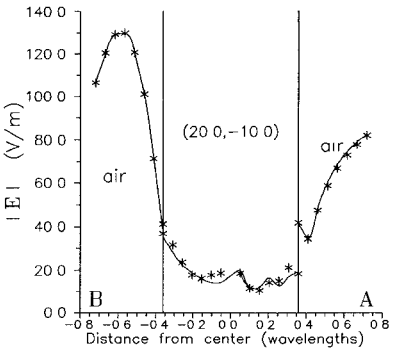

Fig. 5. Amplitude of the total electric field $|\boldsymbol{E}|$ along the BA line at $\theta = 6.4286°$ and $\phi = 45°$ for case 2.

field is discontinuous at the dielectric interfaces, and the finite element solution follows the analytical one very closely. For the specific line BA, the electric field is more discontinuous at the back since, in the region of point B at the front, it is still strongly tangential. Also, the absorption is maximum at the front.

Figs. 6 and 7 show how the error changes in cases 3 and 4 as the ABS is moved outwards. The maximum field error shown is the one described above (12). Fig. 8 shows the amplitude of the total electric field $\boldsymbol{E}$ along the line BA for case 4. As the same mesh density was used inside and outside the dielectric, discretization error is higher inside the dielectric sphere. This is due to the mesh generator used that could only provide the same discretization throughout the region. The average error in the air region was about 1%, while inside the dielectric it was about 2%.

The iterative conjugate gradient method and some of its variants were tried for the solution of the final FE matrix. Most of them failed to converge; when they did, the rate of convergence was too slow: for a 4000 × 4000 matrix, 20 000 iterations were needed. Therefore, the vectorized direct BCS solver was used instead [16]. More details on computational considerations may be found in [5], [12].

V. Conclusion

The open boundary problem of the lossy dielectric sphere scatterer was analyzed using a new simplified functional.

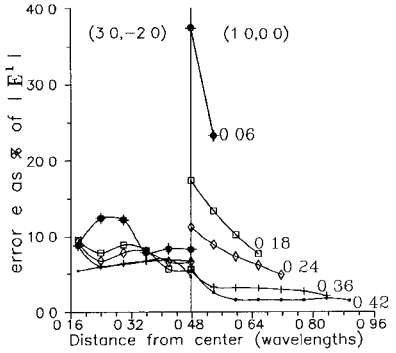

Fig. 6. Solution error versus r, which is the distance from the origin 0. The radius of the dielectric sphere is $R = 0.447\lambda_0$ and its relative permittivity $\epsilon_r = (3.0, -2.0)$. The solution error is the largest value of $e = |\boldsymbol{E}^s_{\mathrm{FEM}} - \boldsymbol{E}^s_{\mathrm{exact}}|$ over the volume modeled, expressed as a percentage of the magnitude of the incident electric field. The numbers at the right end of each curve indicate the distance D in free-space wavelengths (see also Fig. 1).

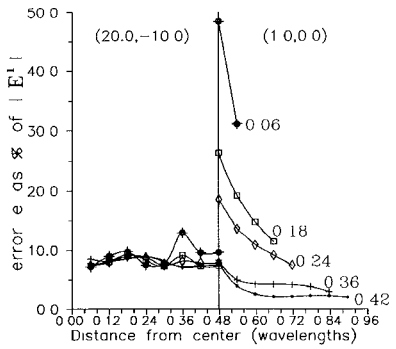

Fig. 7. Solution error versus r, which is the distance from the origin 0. The radius of the dielectric sphere is $R = 0.477\lambda_0$ and its relative permittivity $\epsilon_r = (20.0, -10.0)$. The solution error is the largest value of $e = |\boldsymbol{E}^s_{\mathrm{FEM}} - \boldsymbol{E}^s_{\mathrm{exact}}|$ over the volume modeled, expressed as a percentage of the magnitude of the incident electric field. The numbers at the right end of each curve indicate the distance D in free-space wavelengths (see also Fig. 1).

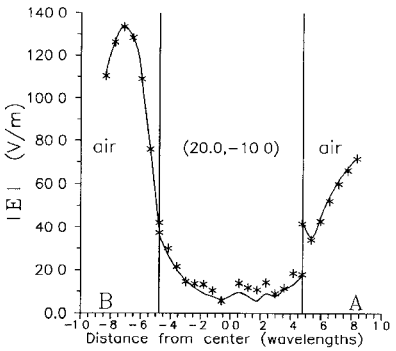

Fig. 8. Amplitude of the total electric field $|\boldsymbol{E}|$ along the BA line at $\theta = 6.4286°$ and $\phi = 45°$ for case 4.

Curvilinear covariant projection elements were used, and also their degenerate forms where needed. Numerical tests suggest that the second-order vector absorbing boundary conditions can effectively absorb outgoing radiation if placed at a distance $D = 0.3\ \lambda_0$ from the scatterer. This also confirms earlier experience with the metallic sphere scatterer. The results give an average error of about 1–2% throughout the meshed region (near-field region). Global far-field parameters may require a much smaller distance D. Although homogeneous

dielectric spheres were tested, the advantage of the FEM lies in the analysis of strongly inhomogeneous objects since no extra interface conditions are required. However, no analytical solutions exist for such problems that could allow a rigorous test of the accuracy of the method.

ACKNOWLEDGMENT

Most of the calculation was done on a Cray Y-MP through the support of Dr. N. Chepurniy from Cray Research Canada. The rest was done on the Cray C98 of the Institut du Développement et des Ressources en Informatique Scientifique (IDRIS), Paris, France. The authors are grateful to all.

REFERENCES

[1] P. P. Silvester and R. L. Ferrari, *Finite Elements for Electrical Engineers*, 2nd ed. Cambridge, U.K.: Cambridge Univ. Press, 1990.
[2] P. Linz, *Theoretical Numerical Analysis*. New York: Wiley, 1979.
[3] J. P. Webb, "Edge elements and what they can do for you," *IEEE Trans. Magn.*, vol. 29, pp. 1460–1465, Mar. 1993.
[4] C. Crowley, P. P. Silvester, and H. Hurwitz, Jr., "Covariant projection elements for 3D vector field problems," *IEEE Trans. Magn.*, vol. 24, pp. 397–400, Jan. 1988.
[5] V. N. Kanellopoulos and J. P. Webb, "3D finite element analysis of a metallic sphere scatterer: Comparison of first and second order vector absorbing boundary conditions," *J. de Physique III France*, vol. 3, pp. 563–572, Mar. 1993.
[6] S. L. Foo and P. P. Silvester, "Finite element analysis of inductive strips in unilateral finlines," *IEEE Trans. Microwave Theory Tech.*, vol. 41, pp. 298–304, Feb. 1993.
[7] J. P. Webb and R. Miniowitz, "Analysis of 3D microwave resonators using covariant-projection elements," *IEEE Trans. Microwave Theory Tech.*, vol. 39, pp. 1895–1899, Nov. 1991.
[8] J. M. Jin and J. L. Volakis, "A finite element-boundary integral formulation for scattering by three-dimensional cavity-backed apertures," *IEEE Trans. Antenn. Propagat.*, vol. 39, pp. 97–104, Jan. 1991.
[9] J. P. Webb and V. N. Kanellopoulos, "Absorbing boundary conditions for the finite element solution of the vector wave equation," *Microwave Opt. Technol. Lett.*, vol. 2, pp. 370–372, Oct. 1989.
[10] V. N. Kanellopoulos and J. P. Webb, "A numerical study of vector absorbing boundary conditions for the finite-element solution of Maxwell's equations," *IEEE Microwave and Guided Wave Lett.*, vol. 1, pp. 325–327, Nov. 1991.
[11] A. Chatterjee, J. M. Jin, and J. L. Volakis, "Edge-based finite elements and vector ABC's applied to 3-D scattering," *IEEE Trans. Antenn. Propagat.*, vol. 41, pp. 221–226, Feb. 1993.
[12] V. N. Kanellopoulos, "Finite elements and vector absorbing boundary conditions in 3-D," Ph.D. dissertation, McGill Univ., Montréal, Canada, 1991.
[13] A. F. Peterson, "Absorbing boundary conditions for the vector wave equation," *Microwave Opt. Technol. Lett.*, vol. 1, pp. 62–64, Apr. 1988.
[14] R. F. Harrington, *Time-Harmonic Electromagnetic Fields*. New York: McGraw-Hill, 1961.
[15] M. R. Spiegel, *Mathematical Handbook of Formulas and Tables*, Schaum's Outline Series. New York: McGraw-Hill, 1968.
[16] The Boeing Extended Mathematical Subprogram Library, Boeing Computer Services, The Boeing Company, 1989.

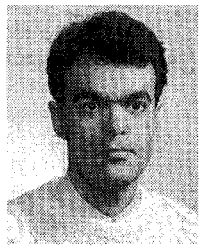

Vassilios N. Kanellopoulos (S'86–S'86–M'86–M'87–S'87–M'91) was born in Thessaloniki, Greece. He received the B.Sc. degree in physics from Aristotle University of Thessaloniki (AUT), Thessaloniki, Greece, and the M.Eng. and Ph.D. degrees in electrical engineering from McGill University, Montréal, Canada, in 1985, 1988, and 1992, respectively.

From 1992–94, he was a postdoctoral fellow with the Laboratoire de Génie Electrique de Paris, Paris, France. He is currently a visiting academic at AUT. His research interests include numerical high-frequency electromagnetics and its application to biomedical problems.

Jon P. Webb (M'83) received the Ph.D. degree from Cambridge University, Cambridge, England, in 1981.

Since 1982 he has been an assistant professor, then an associate professor, in the Department of Electrical Engineering, McGill University, Montreal, Canada. His area of research is computer methods in electromagnetics, especially the application of the finite element method.